

The total electric polarisability is

$$\chi(z) = 2 \sum_{l=0}^{M_l} \sum_{u=0}^{M_u} \int_{uT_b-b}^{uT_b+b} \int_{lT_a-a}^{lT_a+a} \Phi^d(x, y, z) dx dy$$

$$= 2ab \sum_{l=0}^{M_l} \sum_{u=0}^{M_u} \sum_{m=1}^{\infty} \sum_{n=1}^{\infty} \gamma_{mn} [c_{mn}^{lu} \sinh k_{mn}(z+d) + d_{mn}^{lu} \cosh k_{mn}(z+d)] \quad (9)$$

Fig. 2 shows the total electric polarisability $\chi(-d)$ against aperture depth for four different cases which have the same total area. As the individual aperture size becomes smaller, so does the total polarisability. Fig. 3 illustrates the potential distributions for cases (iii) and (iv) of Fig. 2 when $d = 0$. It is seen that the potentials retain almost plateau shapes within the apertures, while sharply

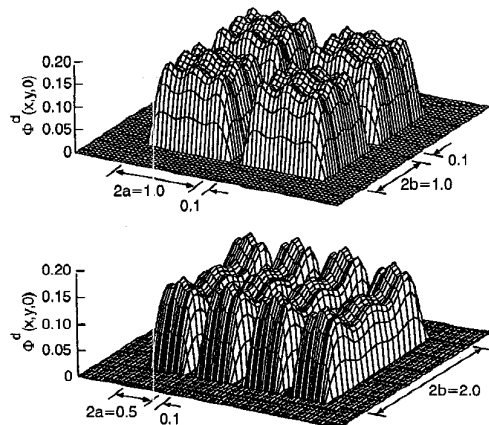


Fig. 3 Potential distributions on apertures

Aperture thickness $d = 0$

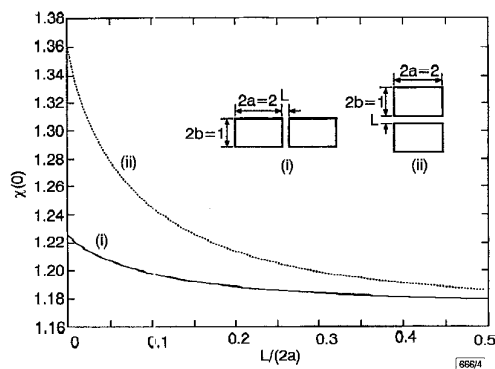


Fig. 4 Behaviour of total electric polarisability $\chi(0)$ against $L/(2a)$

Aperture thickness $d = 0$

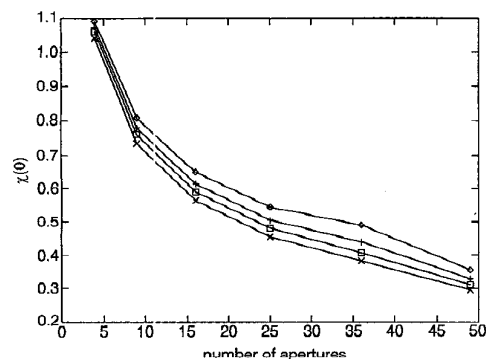


Fig. 5 Behaviour of total electric polarisability $\chi(0)$ against number of apertures

Aperture thickness $d = 0$

—◇— $L = 0.01$ —□— $L = 0.03$
 —+— $L = 0.02$ —×— $L = 0.05$

decreasing near the edges. Fig. 4 shows the behaviour of $\chi(0)$ against the distance between adjacent apertures $L/(2a)$. It is seen that the square-like case (ii) has a higher total polarisability than the other (i). As $L/(2a)$ increases, $\chi(0)$ of (ii) drops faster than that of (i), implying that the mutual interaction between adjacent apertures in (ii) is stronger than in (i). Fig. 5 illustrates $\chi(0)$ against the number of square apertures, N^2 ($N = M_l + 1 = M_u + 1$) when $T_a = T_b$, $a = b$, and $L = T_a - 2a$. The total area of apertures ($4N^2a^2$) is chosen to be 4, thus $a = 1/N$. The distance between apertures, L , is kept very thin; hence, N^2 multiple apertures are approximately regarded as a single aperture, of $a = 1$, covered with thin metallic wire meshes. It is seen that the incident field penetrates less into the wire-meshed apertures as the meshes become more dense. If the interaction between other apertures is ignored, $\chi(0)$ is approximately given by $1.8/N$ which is N^2 times the polarisability of a single aperture with $a = 1/N$. Note that the true $\chi(0)$ is somewhat higher than $1.8/N$.

Conclusion: The behaviour of total polarisability and potential distribution through multiple rectangular apertures is studied in terms of aperture shape parameters. The effects on polarisability of interaction amongst adjacent apertures are discussed.

© IEE 1998

9 June 1998

Electronics Letters Online No: 19981021

H.H. Park and H.J. Eom (Department of Electrical Engineering, Korea Advanced Institute of Science and Technology, 373-1, Kusong Dong, Yuseong Gu, Taejeon, Korea)

Hyo J. Eom: On sabbatical leave at the Department of Electronic and Electrical Engineering, University of Sheffield, Mappin Street, Sheffield, S1 3JD, United Kingdom

References

- 1 McDONALD, N.A.: 'Polynomial approximations for the electric polarisabilities of some small apertures', *IEEE Trans. Microw. Theory Tech.*, 1985, **33**, (11), pp. 1146-1149
- 2 PARK, H.H., and EOM, H.J.: 'Electrostatic potential distribution through a rectangular aperture in a thick conducting plane', *IEEE Trans. Microw. Theory Tech.*, 1996, **44**, (10), pp. 1745-1747

Extension of Kirchhoff method under stationary phase approximation to determination of polarimetric thermal emission of the sea

A. Camps, I. Corbella and J.M. Rius

Wind direction over the sea can be determined from radiometric measurements of the third Stokes parameter (T_U). The Kirchhoff method is extended under the stationary phase approximation to compute the dependence of T_U on frequency, wind speed and incidence angle. Numerical predictions, in agreement with experimental measurements, are presented.

Introduction: Global wind speed maps are computed daily over the oceans from wind scatterometers and vertical/horizontal brightness temperatures. Recent studies have shown that wind direction can also be derived from radiometric measurements of the third Stokes parameter, a very attractive technique since polarimetric radiometers demand less power than wind scatterometers. In this Letter, the Kirchhoff model (KM) under the stationary phase approximation (SPA) is generalised to compute the third Stokes parameter (T_U) and its dependence on frequency, wind speed, angle of incidence, etc. Simple models are included to account for sea foam effects. Numerical results agree with experimental results obtained by other authors.

Basic concepts on polarimetric radiometry: The thermal emission of a surface in a given direction is described by the four element Stokes vector [1]:

$$\begin{bmatrix} T_h \\ T_v \\ T_U \\ T_V \end{bmatrix} = T_s \begin{bmatrix} e_h \\ e_v \\ e_U \\ e_V \end{bmatrix} = C' \begin{bmatrix} \langle E_h E_h^* \rangle \\ \langle E_v E_v^* \rangle \\ 2\mathbf{R}\langle E_v E_h^* \rangle \\ 2\mathbf{I}\langle E_v E_h^* \rangle \end{bmatrix} \quad (1)$$

where T_h and T_v are the horizontal (h) and vertical (v) brightness temperatures, and T_U and T_V are the third and fourth Stokes parameters that account for the correlation between polarisations, respectively. They are related to the surface temperature T_s by their corresponding emissivities e_h , e_v , e_U , and e_V . E_h and E_v are, respectively, the emitted electric fields at horizontal and vertical polarisations, \mathbf{R} and \mathbf{I} are the real and imaginary parts, $\langle \rangle$ is the expectation operator, and C' is a constant.

The emissivities of an irregular surface over the XY plane, at h/v polarisations observed from direction (θ_s, ϕ_s) are related to its scattering properties [2, 3, eqn. 18.30]:

$$e_v(\theta_s, \phi_s) = 1 - \frac{1}{4\pi \cos \theta_s} \iint_{2\pi} \cos \theta_i \left[\gamma_{vvvv}(\theta_s, \phi_s, \theta_i, \phi_i) + \gamma_{vhvh}(\theta_s, \phi_s, \theta_i, \phi_i) \right] d\Omega_i \quad (2)$$

and that of the third and fourth Stokes parameters (polarimetric case) [1]:

$$e_U(\theta_s, \phi_s) = -\frac{1}{4\pi \cos \theta_s} \iint_{2\pi} \cos \theta_i 2 \frac{\mathbf{R}}{\mathbf{I}} [\gamma_{vhvh}(\theta_s, \phi_s, \theta_i, \phi_i) + \gamma_{vvvv}(\theta_s, \phi_s, \theta_i, \phi_i)] d\Omega_i \quad (3)$$

The polarimetric bistatic scattering coefficients $\gamma_{mpq}(\theta_s, \phi_s, \theta_i, \phi_i)$ are related to the polarimetric scattering matrix elements $f_{pq}(\theta_s, \phi_s, \theta_i, \phi_i)$ and the illuminated area A [1].

KM-SPA applied to sea surface roughened by wind: The electric fields scattered at p -polarisation from an undulating surface can be computed by the *KM-SPA* [1], [1-3, eqns.12.23-12.26]:

$$E_p(\theta_s, \phi_s) = E_0 \frac{e^{-jkr}}{r} f_{pq}(\theta_s, \phi_s, \theta_i, \phi_i) = -jE_0 \frac{k}{4\pi} \frac{e^{-jkr}}{r} I_l U_{pq} \quad (4)$$

where E_0 is the amplitude of the incident electric field at q -polarisation, and I_l and U_{pq} are defined in eqns. 12.22-12.36 of [2]. Applying the *KM-SPA* to the anisotropic geometry of the sea surface, Stogryn found that [2, 3, eqns.18.33-18.34]

$$\gamma_{pqpq}(\theta_s, \phi_s, \theta_i, \phi_i) = \frac{1}{\cos \theta_i} \frac{k^2 q^2 |U_{pq}|^2}{2q_x^4 g_x g_y} \times \exp \left[-\frac{1}{2q_x^2} \left(\frac{q_x^2}{g_x^2} + \frac{q_y^2}{g_y^2} \right) \right] \quad (5)$$

where the parameters in eqn. 5 are defined in [3]. It should be pointed out that the U_{pq} terms depend on the Fresnel reflection coefficients for h/v polarisations, that depend on the incidence angle θ_i and the dielectric permittivity of sea water, which in turn depends on the salinity content (S) and temperature (T_s). The g_x^2 and g_y^2 factors in eqn. 5 are the variances of the slopes along the upwind (Y -axis, $\phi = 90^\circ$) and crosswind directions, respectively, and are related to the wind speed at 12.5m height. Wilheit suggested that: (i) the values of the slope variances must be multiplied by a factor $0.3 + 0.02f$ (in gigahertz) for frequencies of < 35 GHz, and (ii) the effect of the sea foam induced by the wind was an isotropic reduction of the reflectivity by a factor $K \approx 0.006 (1 - e^{-0.75(u-7)})$, for wind speeds > 7 m/s, where u is in metres/second. This reflectivity decrease produces an increase in $T_{h/v}$, but a decrease in $T_{U/V}$.

Extension of polarimetric radiometry of KM-SPA to sea surface roughened by wind and comparison with experimental measurements: The polarimetric bistatic scattering coefficients γ_{mpq} can be derived in a similar way as the scattering coefficients (eqn. 5). The results are the same as for eqn. 5, but we replace the term $|U_{pq}|^2$ by $U_{mn} U_{pq}^*$, from which the polarimetric behaviour of the thermal emission can be computed (eqns. 1 and 3). Numerical results with the above model show that T_U has a sinusoidal variation of the

form $T_U(\phi) = T_{U2}(\theta, f, u) \sin(2\phi)$, with zero crossings at 0, 90, 180 and 270°, which may be used to estimate the wind direction, once the wind speed is determined from T_h and T_v . Fig. 1 shows the maximum absolute value of T_U , at $\phi = 45^\circ$, against the incidence angle with respect to nadir, at 19, 37 and 89GHz, and for three different wind speeds at 12.5m. According to these results and experimental evidence reported in [4]: (i) the polarimetric emission behaviour has a weak dependence on frequency, and a very strong dependence on wind speed, and (ii) the sign of the second harmonic of T_U , $T_{U2}(\theta, f, u)$, changes between 45 and 65°, decreasing with increasing wind speeds. Consequently, the sensitivity to wind speed is maximised, without sign ambiguity in ϕ , regardless of its speed, for incidence angles outside the range for which $T_{U2}(\theta, f, u)$ vanishes.

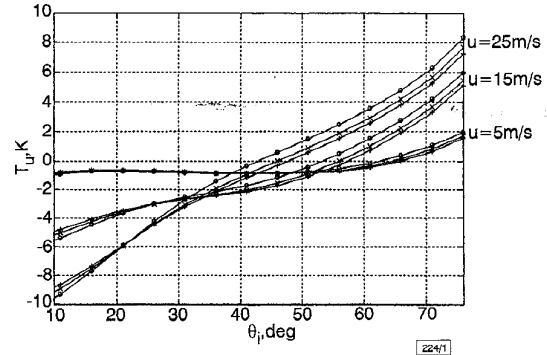


Fig. 1 Maximum amplitude of third Stokes parameter against incidence angle

Wind speed $u = 5, 15$ and 25 m/s at 12.5 m, $S = 33\text{‰}$, $T_s = 25^\circ\text{C}$, $\phi = 45^\circ$
 \bullet 19 GHz
 \times 37 GHz
 \circ 89 GHz

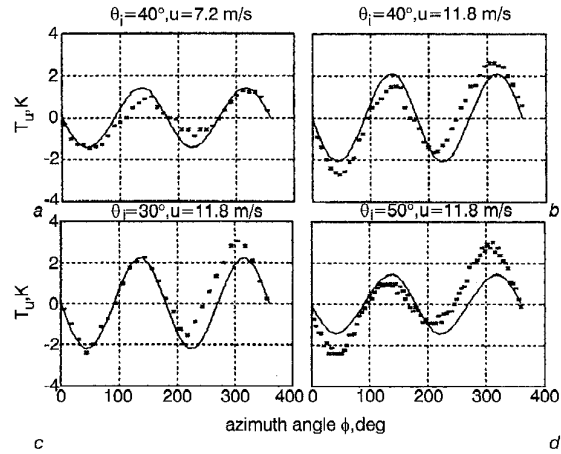


Fig. 2 Comparison of numerical results with experimental measurements [5]

Frequency = 19.35 GHz, wind speed (u) at 5 m, $S = 33\text{‰}$, $T_s = 25^\circ\text{C}$
Fourier coefficients of measured data:

- a $T_{U1} = -0.4$ K, $T_{U2} = -1.1$ K
- b $T_{U1} = -1.0$ K, $T_{U2} = -2.0$ K
- c $T_{U1} = -0.7$ K, $T_{U2} = -2.0$ K
- d $T_{U1} = -1.1$ K, $T_{U2} = -1.8$ K

Fig. 2a and b compares the numerical results, computed with a 33‰ salinity and a sea surface temperature of 25°C, with the measurements reported by Yueh *et al.* [5]. Those measurements were obtained with a 19.35 GHz polarimetric radiometer at $\theta_i = 40^\circ$, and wind speed 7.2 and 11.8 m/s at 5 m height. Owing to the lack of information, atmospheric effects and downward sun radiation polarised through reflection over the sea surface have not been taken into account. The agreement between measured data and the computed values is quite good. The overestimation of $T_U(\phi)$ in the range $[0, 180^\circ]$, and its underestimation in the range $[180^\circ, 360^\circ]$, is due to the presence of a first harmonic of $T_U(\phi)$ of the form $-|T_{U1}(\theta, f, u)| \sin(\phi)$, not predicted by the model. This

asymmetry in $T_U(\Phi)$ is attributed to the particular level of wave asymmetry and foam distribution [1, 6] not modelled. The impact of the first harmonic is more important for incidence angles close to the zero-crossing point of $T_{V2}(\theta, f, u)$ (Fig. 1). This effect is shown in Fig. 2c and d, at incidence angles of 30 and 50°. Finally, it should be pointed out that the value of T_V computed with this model is zero. Reported experimental data [4] reveal that in fact T_V does not vanish, but it is much smaller than T_U .

Conclusions: An extension of the *KM-SPA* method that allows the computation of the polarimetric emission characteristics of the sea surface roughened by the wind, including a simple isotropic model to account for the effect of sea foam, has been presented. Numerical results are in good agreement with reported experimental data. It has been shown that, depending on wind speed, at some incidence angles the second harmonic of the third Stokes parameter vanishes, as reported from experiments performed by other authors. The model also predicts the small dependence of T_U on frequency and its strong dependence on wind speed, and can be used to optimise the design of experimental setups, as well as to interpret data to determine wind speed.

Acknowledgment: This work has been supported by the Spanish Comisión Interministerial de Ciencia y Tecnología (CICYT TIC 96/0879).

© IEE 1998

1 May 1998

Electronics Letters Online no: 19981055

A. Camps, I. Corbella and J.M. Rius (Department of Signal Theory and Communications, Universitat Politècnica de Catalunya, Campus Nord, Mòdul D4, c/Jordi Girona 1-3, 08034 Barcelona, Spain)

References

- 1 YUEH, S.H., KWOK, R., LI, F.K., NGHIEM, S.V., WILSON, W.J., and KONG, J.A.: 'Polarimetric passive remote sensing of ocean wind vectors', *Radio Science*, 1994, **29**, (4), pp. 799-814
- 2 ULABY, F.T., MOORE, R.K., and FUNG, A.K.: 'Microwave remote sensing. Active and passive' (Artech House, 1982), Vol II, pp. 925-931
- 3 ULABY, F.T., MOORE, R.K., and FUNG, A.K.: 'Microwave remote sensing. Active and passive' (Artech House, 1986), Vol III, pp. 1442-1443
- 4 YUEH, S.H., WILSON, W.J., LI, F.K., NGHIEM, S.V., and RICKETTS, W.B.: 'Polarimetric brightness temperatures of sea surfaces measured with aircraft K- and Ka-band radiometers', *IEEE Trans. Geosci. Remote Sens.*, 1997, **35**, (5), pp. 1177-1187
- 5 YUEH, S.H., WILSON, W.J., LI, F.K., NGHIEM, S.V., and RICKETTS, W.B.: 'Polarimetric measurements of sea surface brightness temperatures using an aircraft K-band radiometer', *IEEE Trans. Geosci. Remote Sens.*, 1995, **33**, (1), pp. 85-92
- 6 KUNKEE, D.B., and CASIEWSKI, A.J.: 'Broadband phenomena in oceanic passive wind direction signatures: The sensitivity to wave asymmetry, foam, and atmospheric profile'. Proc. IGARSS, 1996, pp. 1129-1131

Decomposition co-ordination artificial neural network for satellite broadcast scheduling

T. Tambouratzis

An artificial neural network is presented which solves the satellite broadcast scheduling problem in parallel. The problem is decomposed into sub-networks, which are co-ordinated employing lateral inhibition. The resulting solutions are valid, correct and optimal, whereby maximal satellite broadcasting is accomplished.

Introduction: The satellite communication industry has grown rapidly in the last three decades, one of its major applications being telecommunications. A satellite communication system (SCS) is characterised by (i) a number of satellites orbiting the earth, (ii) a number of stationary ground terminals, and (iii) a number of communication requests, one for each satellite specifying how long the satellite must broadcast in order for the communication task to be

executed (a satellite can broadcast to a terminal only if the former is visible from the latter).

Depending on the altitude of satellite orbit, high- and low-altitude SCSs exist. Low-altitude SCSs offer the advantages of fuller communication coverage, smaller propagation delays, reduced power requirements and portable antennas. Since, however, the satellites are not always visible from the ground terminals, a handover between satellites is necessary in order for the communication requests to be satisfied. This handover constitutes the satellite broadcast scheduling (SBS) problem for low-altitude SCSs.

An artificial neural network (ANN) based on harmony theory [3] is proposed for solving SBS (also see [1, 2]). SBS is decomposed into sub-networks that are co-ordinated via lateral inhibition. The ANN provides valid and correct solutions for which maximal satellite broadcasting is effected.

Problem formulation: An SBS problem involves J ground terminals t_j ($1 \leq j \leq J$) and I satellites s_i ($1 \leq i \leq I$) whose communication requests must be satisfied over time T . By discretising T into K time slots T_k ($1 \leq k \leq K$):

- (1) $S_{j,k}$ represents SBS; $S_{jk} = 1$ if s_j is visible from t_j at T_k (0 otherwise).
- (2) R_j^T expresses the communication requests; R_i equals the number of time slots during which s_i must broadcast.
- (3) $C_{i,j,k}$ represents a solution of SBS; $C_{ijk} = 1$ if s_i broadcasts to t_j at T_k (0 otherwise).

For C to constitute a valid and correct solution of SBS, communication must be appropriately assigned between all s_i and t_j over all T_k :

- (i) **Validity** $\forall T_k$
 - a s_i can broadcast to t_j only if it is visible from t_j .
 - b s_i can broadcast to at most one terminal.
 - c t_j can communicate with at most one satellite.
- (ii) **Correctness** $\forall R_i$

$$R_i = \sum_{j=1}^J \sum_{k=1}^K C_{ijk} \quad (1)$$

In practice, it is of interest to accomplish maximal broadcasting; eqn. 1 is replaced by

$$R_i \leq \sum_{j=1}^J \sum_{k=1}^K C_{ijk} \quad \text{and} \quad \text{maximise} \left\{ \sum_{i=1}^I \sum_{j=1}^J \sum_{k=1}^K C_{ijk} \right\} \quad (2)$$

Proposed ANN approach: The ANN used for validly, correctly and optimally solving SBS is based on harmony theory [3] and is characterised by:

- (i) Two layers of binary nodes and connections between nodes of different layers. The nodes of the lower layer encode local problem states and those of the upper layer encode the constraints between local states. The sign of each connection denotes whether the encoded constraint supports or inhibits the encoded local state.
- (ii) Positive integer strengths σ to the nodes of the upper layer expressing the priority level of the encoded constraints.
- (iii) Repeated node updates until ANN settling.
- (iv) Maximal constraint satisfaction, realised by maximisation of the number of active nodes of the upper layer. During ANN settling, the consensus (harmony) function guides the ANN towards a state composed of the maximum number of active nodes of the upper layer.

Problem decomposition is performed; one sub-network (j, k) is created for each combination of t_j and T_k only if $N_{jk} > 0$ (N_{jk} is the number of satellites that are visible from t_j at T_k). Sub-network (j, k) comprises:

- (1) N_{jk} nodes in the lower layer enforcing (i)a. Each node encodes one s_i^* for which $S_{i,j,k}^* = 1$.
- (2) N_{jk} nodes in the upper layer. Each node encodes the constraints that apply to s_i^* if $C_{i,j,k}^* = 1$.
- (3) Full connectivity enforcing (i)b. For each node of the upper layer, one positive and $N_{jk} - 1$ negative connections appear to the nodes of the lower layer.

The sub-networks are co-ordinated via:

- (4) Sparse lateral inhibition enforcing (i)c. For every visible s_i^* and every pair of sub-networks (j, k) and (j^*, k^*), $j^* \neq j$, negative connections extend from the node of the upper layer of (j, k)